CRYSTAL GROWTH & DESIGN
2006
VOL. 6, NO. 6
1291−1303

Simulation of Mixing Effects in Antisolvent Crystallization Using a Coupled CFD-PDF-PBE Approach

Xing Yi Woo,[†,‡] Reginald B. H. Tan,[‡,§] Pui Shan Chow,[§] and Richard D. Braatz*[,†]

Department of Chemical and Biomolecular Engineering, University of Illinois at Urbana-Champaign, 600 South Mathews Avenue, Urbana, Illinois 61801, Department of Chemical and Biomolecular Engineering, National University of Singapore, 4 Engineering Drive 4, Singapore 117576, and Institute of Chemical and Engineering Sciences, 1 Pesek Road, Jurong Island, Singapore 627833

Received July 1, 2005; Revised Manuscript Received February 27, 2006

ABSTRACT: Antisolvent crystallization is widely used in the production of pharmaceuticals. Although it has been observed experimentally that the crystal size distribution is strongly influenced by the imperfect mixing of the antisolvent with the solution, these effects have not been adequately quantified. In this work, a turbulent computational fluid dynamics (CFD) code was coupled with a multienvironment probability density function (PDF) model, which captures the micromixing in the subgrid scale, and the population balance equation, which models the evolution of the crystal size distribution. The population balance equation (PBE) was discretized along the internal coordinate using a high-resolution central scheme. The presence of solids was addressed by treating the suspension as a pseudo-homogeneous phase with a spatial variation in the effective viscosity. This coupled CFD-PDF-PBE algorithm was applied to an antisolvent crystallization process in an agitated semibatch vessel, where the rising liquid level was modeled by a dynamic mesh. The effects of agitation speed, addition mode, and scale-up on the local primary nucleation and size-dependent growth and dissolution rates, as well as the crystal size distribution, were numerically investigated.

Introduction

Antisolvent crystallization is used widely in the pharmaceutical industry. This enables the crystallization of thermally sensitive pharmaceuticals without introducing large temperature changes in the process.[1,2] Current state-of-the-art crystallization technology such as impinging jet crystallizers utilizes high-intensity mixing of the antisolvent and the solution to produce crystals smaller than 25 μm with improved bioavailability and increased dissolution rates,[3−5] which, at the same time, reduces the undesirable effects of milling.[6,7] Various experimental studies of antisolvent crystallization in an agitated semibatch vessel indicate that the crystal size distribution (CSD) depends strongly on the operating conditions, such as agitation rate, mode of addition (direct or reverse), addition rate, solvent composition, and size of the crystallizer.[5,8−20] The polymorphic or pseudopolymorphic form can also depend on the operating conditions.[21−26]

Most variations in the operating conditions have a direct influence on the mixing of the antisolvent and the solution, which affects the localized supersaturation and, thus, the crystal product. Because the dependence of nucleation and growth rates on supersaturation is highly system specific, determining the optimal process conditions that produce the desirable crystal product can require numerous bench-scale laboratory experiments, which might not be optimal after the scale-up of the crystallizer, as the mixing effects and spatial distribution of supersaturation can be vastly different.[27,28] In addition, control strategies developed on the basis of the assumption of perfect mixing may not result in the intended crystal product when implemented at the industrial scale.[29] A pressing issue for the pharmaceutical industry is the regulatory requirement of consistency in the various chemical and physical properties of the crystals, including the CSD.[30] Such concerns motivate the development of a computational model to simulate the antisolvent crystallization process to quantify the effects of mixing on the product crystal characteristics such as the CSD, which determines the bioavailability of the drug and efficiency of downstream processes (e.g., filtration and drying).[31]

The modeling of well-mixed crystallizers involves the computation of the population balance equation (PBE) together with the material balance equations for each species in solution. Numerous numerical techniques that compute the full CSD have been used to model well-mixed batch, semibatch, or continuous crystallizers.[32−45] To account for nonideal mixing, the PBE has to be coupled with the transport equations of mass, momentum, and energy.[46] One approach is to couple turbulent computational fluid dynamics (CFD) codes with the solution of the PBE, and most of the literature studies focus on reactive crystallization systems.[47−50] A recent paper by Choi et al.[51] models the antisolvent crystallization process in a jet Y-mixer using a hybrid CFD-PBE approach but neglects the micromixing effects. Compartmental modeling, where the crystallizer is divided into a number of well-mixed compartments connected by interchanging flows, is a less computationally intensive approach.[52] One strategy is to compartmentalize the crystallizer into regions that are, to some degree, homogeneous in properties of interest (e.g., suspension density, energy dissipation, supersaturation), as determined by CFD simulations.[53] However, compartmental modeling oversimplifies the flow field and, most importantly, it loses the spatial resolution of the supersaturation and turbulent energy dissipation distribution in the crystallizer.

Subsequently, the effects of micromixing have been included in coupled CFD-PBE computations to model turbulent precipitators[54−62] (here, the term "precipitation" is reserved to refer to reactive crystallization), in which a variety of methods were used to approximate the probability density function (PDF),[63,64] which is a statistical description of the fluctuating scalars (e.g., species concentrations) at a subgrid scale. The solution of the PBE was obtained by the method of moments, which only computes the average and aggregate properties of the crystalline phase. Recently, a supercritical antisolvent crystallization process was modeled using this strategy.[65]

* To whom correspondence should be addressed. Tel: 217-333-5073. Fax: 217-333-5052. E-mail: braatz@uiuc.edu.
† University of Illinois at Urbana-Champaign.
‡ National University of Singapore.
§ Institute of Chemical and Engineering Sciences.

10.1021/cg0503090 CCC: $33.50
Published on Web 04/20/2006

An alternative method used to include micromixing effects in precipitation models utilizes a multizonal approach in a Lagrangian framework,[66] in which the precipitator is divided into a few segregated zones (e.g., feed/reactant zone, mixed/reaction zone, contact zone, bulk zone). The volume change of the zones and the material exchange between the zones are determined by the meso- and micromixing rates.[67] The reduction in the computational expense by eliminating the direct linkage to CFD computations enabled the simulation of the PBE equation for the full CSD.[68−72] In some instances, additional approximations included the confinement of nucleation and crystal growth to certain zones. A variation of this approach by Kresta et al.[73] used a multiscale Eulerian−Lagrangian framework to couple the zones in the bulk fluid, governed by long time and length scales, with the discretized volumes of the feed plume, governed by short time and length scales.

Compartmental modeling, coupled to the solution of the PBE for the full particle size and shape distribution, also has been applied to cooling crystallization and polymerization processes.[74] The simulations of CSD by Ma et al.[29,75] and Sha and Palosaari[76] took into account the spatial distribution of the solid particles of different sizes, which is important when the crystalline phase is much denser than the solution. This was an advance over the earlier works in modeling crystallizers that assumed that the solid particles follow the liquid streamlines, which avoided the use of multiphase models. In contrast, the coupling of CFD, PBE, and multiphase models has been an ongoing effort in the modeling of bubble size distribution as a result of coalescence and breakup in gas−liquid processes (e.g. bioreactor).[77,78]

On the basis of these past efforts, it is apparent that the next step in modeling crystallizers requires a higher resolution of the flow field in order to establish a better understanding of the interactions between hydrodynamics and crystal nucleation and growth, and the impact on the CSD. In this contribution, an approach to couple the CFD computations to the solution of the PBE to simulate the full CSD and the solution of the PDF that describes the local fluctuations in the turbulent flow field are presented. The development of this algorithm also is motivated by emerging sensor technologies, which allow the in situ measurement of the solution concentration and the full CSD as a function of time[79] and space.[80−83] Thus, a complete validation of the coupled simulation algorithm is feasible, which would provide support for any theoretical understandings or conclusions made on the basis of the simulation results. Although direct numerical simulations (DNS) can resolve all flow structures of the turbulent flow and avoid the prediction of the PDF, the application of DNS in a highly turbulent flow in a full-scale reactor with chemical reactions and crystallization is still computationally intractable.[84,85] Instead, here the full CSD is solved numerically using the high-resolution, finite-volume, semidiscrete central scheme proposed by Kurganov and Tadmor[86] and the micromixing is modeled by a multienvironment presumed-PDF model.[84] This approach can be integrated within commercially available CFD codes, in which the additional models are simulated within the CFD solver. This coupled algorithm is applied to simulate the antisolvent crystallization of paracetamol from an acetone−water mixture[12] in a semibatch stirred vessel. The rise in liquid level is captured by a dynamic mesh, which is commonly used for aeroelastic and free surface simulations.[87,88] The presence of solids is modeled by treating the slurry as a pseudo-homogeneous fluid with a spatial distribution of effective viscosity that depends on the local solids fraction.[89] The effects of agitation rate, addition mode, and scale-up on the transient CSD are investigated.

Integration of CFD, PBE, and PDF Models

This section describes the numerical methods used to compute (1) the PBE for the evolution of CSD and (2) the PDF of the local turbulent fluctuations, which are directly integrated into a CFD code. In addition, the expressions for the crystallization kinetics and the effective viscosity are presented.

High-Resolution, Finite-Volume, Semidiscrete Central Schemes. High-resolution finite-volume methods have been investigated primarily in the applied mathematics and computational physics literature.[90] These methods provide high accuracy for simulating hyperbolic conservation laws while reducing numerical diffusion and eliminating nonphysical oscillations that can occur with classical methods. Being in the class of finite volume methods, such methods are conservative, which ensures the accurate tracking of discontinuities and preserves the total mass within the computational domain subject to the applied boundary conditions. Another advantage is that these numerical schemes can be easily extended to solve multidimensional and variable-coefficient conservation laws.

High-resolution central schemes for nonlinear conservation laws, starting from the NT scheme of Nessyahu and Tadmor,[91] have the advantages of retaining the simplicity of the Riemann-solver-free approach, while achieving at least second-order accuracy. Kurganov and Tadmor[86] and Kurganov et al.[92] extended the NT scheme to reduce numerical viscosity (nonphysical smoothing of the numerical solution) arising from discrete approximations of the advection term. This KT high-resolution finite-volume central scheme accumulates less dissipation for a fixed Δy as compared to the NT scheme and can be used efficiently with small time steps, since the numerical viscosity is independent of $1/\Delta t$. The limiting case, $\Delta t \rightarrow 0$, results in the second-order semidiscrete version. In addition, the KT method satisfies the scalar total-variation-diminishing (TVD) property with minmod reconstruction, which implies that the nonphysical oscillations that occur with many second-order accurate numerical methods cannot occur with this method. The KT semidiscrete scheme is particularly effective when combined with high-order ODE solvers for the time evolution.

Consider the nonlinear conservation law

$$\frac{\partial}{\partial t}u(y,t) + \frac{\partial}{\partial y}q(u(y,t)) = 0 \tag{1}$$

The semidiscrete central scheme of Kurganov and Tadmor[86] is classified as a finite-volume method, since it involves keeping track of the integral of u over each grid cell. The use of cell averages

$$u_j(t) = \frac{1}{\Delta y}\int_{y_{j-1/2}}^{y_{j+1/2}} u(y,t)\,\mathrm{d}y \tag{2}$$

to represent computed values, where $\Delta y = y_{j+1/2} - y_{j-1/2}$, ensures that the numerical method is conservative. The second-order semidiscrete scheme admits the conservative form

$$\frac{\mathrm{d}}{\mathrm{d}t}u_j(t) = -\frac{H_{j+1/2}(t) - H_{j-1/2}(t)}{\Delta y} \tag{3}$$

with the numerical flux

$$H_{j+1/2}(t) := \frac{q(u_{j+1/2}{}^{+}(t)) + q(u_{j+1/2}{}^{-}(t))}{2} - \frac{a_{j+1/2}}{2}[u_{j+1/2}{}^{+}(t) - u_{j+1/2}{}^{-}(t)] \tag{4}$$

and the intermediate values given by

$$u_{j+1/2}^{+} := u_{j+1}(t) - \frac{\Delta y}{2}(u_y)_{j+1}(t)$$

$$u_{j+1/2}^{-} := u_j(t) + \frac{\Delta y}{2}(u_y)_j(t) \tag{5}$$

while the local propagation of speeds, for the scalar case, is

$$a_{j+1/2}(t) := \max_{u\in[u_{j+1/2}^{-}(t),u_{j+1/2}^{+}(t)]} |q'(u_{j+1/2}^{-}(t))| \tag{6}$$

The derivatives are approximated with the minmod limiter

$$(u_y)_j^n := \text{minmod}\left(\theta\frac{u_j^n - u_{j-1}^n}{\Delta y}, \frac{u_{j+1}^n - u_{j-1}^n}{2\Delta y}, \theta\frac{u_{j+1}^n - u_j^n}{\Delta y}\right) \tag{7}$$

$$1 \le \theta \le 2$$

which is defined as

$$\text{minmod}(\alpha_1, \alpha_2, ...) = \begin{cases} \min_i\{\alpha_i\} & \text{if } \alpha_i > 0\ \forall i \\ \max_i\{\alpha_i\} & \text{if } \alpha_i < 0\ \forall i \\ 0 & \text{otherwise} \end{cases} \tag{8}$$

Selecting the value of $\theta = 1$ results in nonphysical smoothing of the numerical solution. A value of $\theta = 2$ results in minimal nonphysical smoothing but can introduce some nonphysical oscillation. The value $\theta = 1.5$ is commonly selected to trade off minimizing the amount of nonphysical dissipation/smoothing with minimizing nonphysical oscillation. The reader is referred to the references in this section for more details on such limiters.

Coupling the PBE to the CFD Algorithm. A spatially inhomogeneous crystallization process can be described by the population balance equation (PBE):[46,93]

$$\frac{\partial f}{\partial t} + \sum_i \frac{\partial[G_i(r_i,c,T)f]}{\partial r_i} + \sum_i \left\{\frac{\partial[v_i f]}{\partial x_i} - \frac{\partial}{\partial x_i}\left[D_t\frac{\partial f}{\partial x_i}\right]\right\} = B(f,c,T)\prod_i \delta(r_i - r_{i0}) + h(f,c,T) \tag{9}$$

where the particle number density function (f) is a function of external coordinates (x_i), internal coordinates (r_i), and time (t). The rates of growth (G_i) and nucleation (B) are functions of the vector of solution concentrations (c) and the temperature (T), and for size-dependent growth, G_i also varies with r_i. The Dirac delta function is δ. The term h represents the creation and destruction of crystals due to aggregation, agglomeration, and breakage. As the solution concentrations and temperature vary with spatial position and time, eq 9 must be solved together with the bulk transport equations for mass, energy, momentum, and turbulence to obtain $f(x,r,t)$, $c(x,t)$, $T(x,t)$, the velocity field $v(x,t)$, and the local turbulent diffusivity $D_t(x,t)$. This enables the determination of the effects of the localized solution environment on the nucleation and growth rates, as well as on the CSD. With v and D_t being obtained by solving the momentum and turbulence conservation equations of the liquid phase, respectively, eq 9 assumes that the particles follow the streamlines in the flow field.[46] This is a good approximation for organic pharmaceutical crystals, where the density is close to the liquid phase, and for primary nucleation in a crystallizer for short times. The approximation becomes less accurate as the crystals increase in size.

High-resolution finite-volume methods can be utilized to solve the PBE, due to the similarity of its mathematical structure to that of hyperbolic conservation equations. Recently, Gunawan et al.[33] and Ma et al.[29,41,75] had demonstrated the capability of using such methods to numerically solve multidimensional PBEs that simulate the evolution of crystal size and shape distribution. The following will briefly present the application of the high-resolution finite-volume semidiscrete central scheme to the PBE. The main advantage of using the high-resolution central scheme to discretize the growth term is that its second-order accuracy allows the use of a larger Δr, while retaining the same numerical accuracy obtained from first-order methods (e.g., upwind method). This is important, because the number of transport equations that can be solved in the CFD algorithm is limited. Moreover, the method does not produce spurious oscillations in the solution, which are common in second-order methods such as Lax−Wendroff. Another advantage of using the high-resolution central scheme is that the numerical dissipation depends on Δr but not $1/\Delta t$. This is essential due to the fact that, in most cases, very small time steps, much smaller than that limited by the Courant−Friedrichs−Lewy (CFL) condition, is required to resolve the turbulent flow and concentration field in the CFD computation. Hence, this method avoids any additional numerical dissipation due to using small Δt. Although the approach taken here is applicable to the general equation (9), the subsequent equations will focus on the case of primary nucleation and size-dependent growth along one internal principal axis, as this will simplify the presentation and these assumptions are consistent with the crystallization system simulated in this paper.

Focusing first only on the first two terms of eq 9, the following semidiscrete PBEs are obtained after integrating over r over each cell and canceling terms:

$$\frac{d}{dt}f_j(t) = \begin{cases} -\frac{1}{\Delta r}\left\{G_{j+1/2}\left[f_j(t) + \frac{\Delta r}{2}(f_r)_j(t)\right] - G_{j-1/2}\left[f_{j-1}(t) + \frac{\Delta r}{2}(f_r)_{j-1}(t)\right]\right\} & G > 0\ (\Delta c > 0)\ \text{(crystal growth)} \\ -\frac{1}{\Delta r}\left\{G_{j+1/2}\left[f_{j+1}(t) - \frac{\Delta r}{2}(f_r)_{j+1}(t)\right] - G_{j-1/2}\left[f_j(t) - \frac{\Delta r}{2}(f_r)_j(t)\right]\right\} & G < 0\ (\Delta c < 0)\ \text{(crystal dissolution)} \end{cases} \tag{10}$$

where f_j is the cell-averaged population density, based on eq 2, and the derivatives, $(f_r)_j$, are approximated by the minmod limiter (eqs 7 and 8). Note that the growth rates are evaluated at the end points of each grid cell. The nucleation term is included in the cell corresponding to the nuclei size by averaging the nucleation rate (the number of nuclei per unit time per unit volume) over the cell width, $B/\Delta r$. The computation of the average population density for the first grid cell, f_1, requires the values of f_0 and f_{-1}, which are fictitious points with population densities of zero at all times. At the other end, the computation of f_N in the last grid cell assumes that $f_{N+1} = f_{N+2} = f_N$ at all times, which is known as the absorbing boundary condition.[90]

To couple the semidiscrete PBE with the CFD algorithm, eq 10 is rewritten on a mass basis so that the set of crystals within each grid cell is treated as a separate species. Thus, when this equation is coupled with the transport equations of other species present in the system (solute, solvent, and antisolvent), also written on a mass basis, the overall mass balance of the system is also satisfied. The cell-averaged crystal mass can be evaluated as

$$f_{w,j} = \rho_c k_v \int_{r_{j-1/2}}^{r_{j+1/2}} r^3 f_j \, dr = \frac{\rho_c k_v f_j}{4}((r_{j+1/2})^4 - (r_{j-1/2})^4) \quad (11)$$

and the transport equation for crystal mass between size $r_{j-1/2}$ and $r_{j+1/2}$ is

$$\frac{d}{dt} f_{w,j} + \sum_i^3 \left\{ \frac{\partial [v_i f_{w,j}]}{\partial x_i} - \frac{\partial}{\partial x_i}\left[D_t \frac{\partial f_{w,j}}{\partial x_i} \right] \right\} = \begin{cases} \frac{\rho_c k_v}{4\Delta r}\left[(r_{j+1/2})^4 - (r_{j-1/2})^4 \right] \times \\ \left\{ -G_{j+1/2}\left[f_j + \frac{\Delta r}{2}(f_r)_j \right] + G_{j-1/2}\left[f_{j-1} + \frac{\Delta r}{2}(f_r)_{j-1} \right] + \underbrace{B}_{j=0} \right\} & \Delta c > 0 \\ \frac{\rho_c k_v}{4\Delta r}\left[(r_{j+1/2})^4 - (r_{j-1/2})^4 \right] \times \\ \left\{ -G_{j+1/2}\left[f_{j+1} - \frac{\Delta r}{2}(f_r)_{j+1} \right] + G_{j-1/2}\left[f_j - \frac{\Delta r}{2}(f_r)_j \right] \right\} & \Delta c < 0 \end{cases} \quad (12)$$

Equation 12 can be directly incorporated into the CFD code as a transport equation when micromixing effects are not important, such that the right-hand side is treated as an additional source term. A corresponding source term is added to the solute transport equation to account for its depletion due to nucleation and crystal growth or its increment due to crystal dissolution, which is a negative sum of eq 12 for $j = 1, ..., N$.

Multienvironment Presumed-PDF Model. A multienvironment CFD micromixing model, also known as the finite-mode PDF method, is used to model the micromixing effects.[84] In this approach, each computational cell in the CFD grid is divided into N_e different probability modes or environments, which correspond to a discretization of the presumed composition PDF into a finite set of δ functions:

$$f_\phi(\psi;\mathbf{x},t) = \sum_{n=1}^{N_e} p_n(\mathbf{x},t) \prod_{\alpha=1}^{N_s} \delta[\psi_\alpha - \langle \phi_\alpha \rangle_n(\mathbf{x},t)] \quad (13)$$

where f_ϕ is the joint PDF of all scalars, N_s is the total number of scalars (species), p_n is the probability of mode n or volume fraction of environment n, and $\langle \phi_\alpha \rangle_n$ is the mean composition of scalar α corresponding to mode n. The weighted concentration is defined as

$$\langle \mathbf{s} \rangle_n \equiv p_n \langle \phi \rangle_n \quad (14)$$

The transport of probability and species in inhomogeneous flows is modeled by

$$\frac{\partial \mathbf{p}}{\partial t} + \sum_i \left[\langle v_i \rangle \frac{\partial \mathbf{p}}{\partial x_i} - \frac{\partial}{\partial x_i}\left(D_t \frac{\partial \mathbf{p}}{\partial x_i} \right) \right] = \mathbf{G}(\mathbf{p}) + \mathbf{G_s}(\mathbf{p}) \quad (15)$$

$$\frac{\partial \langle \mathbf{s} \rangle_n}{\partial t} + \sum_i \left[\langle v_i \rangle \frac{\partial \langle \mathbf{s} \rangle_n}{\partial x_i} - \frac{\partial}{\partial x_i}\left(D_t \frac{\partial \langle \mathbf{s} \rangle_n}{\partial x_i} \right) \right] = \mathbf{M}^n(\mathbf{p}, \langle \mathbf{s} \rangle_1, \langle \mathbf{s} \rangle_{N_e}) + \mathbf{M_s}^n(\pi, \langle \mathbf{s} \rangle_1, ..., \langle \mathbf{s} \rangle_{N_e}) + p_n \mathbf{S}(\langle \phi \rangle_n) \quad (16)$$

where $\mathbf{G}$ and $\mathbf{M}^n$ are the rates of change of $\mathbf{p} = [p_1 p_2 ... p_N]$ and $\langle \mathbf{s} \rangle_n$ due to micromixing, respectively, $\mathbf{G}_s$ and $\mathbf{M_s}^n$ are additional micromixing terms to eliminate the spurious dissipation rate in the mixture-fraction-variance transport equation (for details see ref 84), and $\mathbf{S}$ is the chemical source term. The conservation of probability requires that

$$\sum_{n=1}^{N} p_n = 1 \quad (17)$$

and

$$\sum_{n=1}^{N_e} G_n(\mathbf{p}) = 0 \quad (18)$$

The mean compositions of the scalars are given by

$$\langle \phi \rangle = \sum_{n=1}^{N_e} p_n \langle \phi \rangle_n = \sum_{n=1}^{N_e} \langle \mathbf{s} \rangle_n \quad (19)$$

and, since the means remain unchanged by micromixing, the following must be satisfied:

$$\sum_{n=1}^{N_e} \mathbf{M}^n(\mathbf{p}, \langle \mathbf{s} \rangle_1, ..., \langle \mathbf{s} \rangle_{N_e}) = 0 \quad (20)$$

The simulations in this paper utilize a three-environment model, as shown in Figure 1. This approach was used by Marchisio et al.[57−59] to model precipitation, who used the method of moments to model the average properties of the crystalline phase. They suggested that three environments are sufficient in capturing the micromixing effects in nonpremixed flows with satisfactory accuracy. The extension to a larger number of environments is possible,[60,62,84] but at a larger computational expense, since one set of semidiscrete PBE has to be solved in each mixed environment. An advantage of using the multienvironment PDF model instead of other micromixing models is that it can be easily incorporated into existing CFD codes, in which the transport equations (15) and (16) can be computed directly by the CFD solver. Since the compositions in environments 1 and 2 are known on the basis of the feed and initial conditions, eq 16 will be applied to all species in environment 3 only, which includes the solute, the solvent, the antisolvent, and the crystal mass in each grid cell of the semidiscrete PBE. Furthermore, eq 16 is used to evaluate the mixture fraction in environment 3 (which represents the relative fractions of fluids from environments 1 and 2), $\langle \xi \rangle_3$, while the mixture fractions in environments 1 and 2 are $\langle \xi \rangle_1 = 1$ and $\langle \xi \rangle_2 = 0$, respectively. With $N_e = 3$, it is possible to simulate the mean, the variance, and the skewness of the mixture fraction correctly.

The micromixing terms are given by[84]

model variable	$\mathbf{G}$, $\mathbf{M}^n$	$\mathbf{G_s}$, $\mathbf{M_s}^n$
p_1	$-\gamma p_1(1-p_1)$	$\gamma_s p_3$
p_2	$-\gamma p_2(1-p_2)$	$\gamma_s p_3$
p_3	$\gamma[p_1(1-p_1) + p_2(1-p_2)]$	$-2\gamma_s p_3$
$\langle \mathbf{s} \rangle_3$	$\gamma[p_1(1-p_1)\langle \phi \rangle_1 + p_2(1-p_2)\langle \phi \rangle_2]$	$-\gamma_s p_3(\langle \phi \rangle_1 + \langle \phi \rangle_2)$

$$\gamma = \frac{\epsilon_\xi}{p_1(1-p_1)(1-\langle \xi \rangle_3)^2 + p_2(1-p_2)\langle \xi \rangle_3^2}$$

$$\gamma_s = \frac{2D_t}{(1-\langle \xi \rangle_3)^2 + \langle \xi \rangle_3^2} \frac{\partial \langle \xi \rangle_3}{\partial x_i} \frac{\partial \langle \xi \rangle_3}{\partial x_i}$$

$$\langle \xi'^2 \rangle = p_1(1-p_1) - 2p_1 p_3 \langle \xi \rangle_3 + p_3(1-p_3)\langle \xi \rangle_3^2$$

where $\langle \phi \rangle_n$ is evaluated using eq 19. The value of p_3 can also be determined from eq 17, but its value can be erroneous when $p_1 + p_2$ is close to 1, due to numerical errors. For a fully

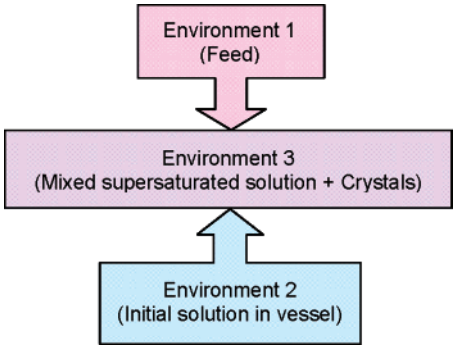

Figure 1. Three-environment micromixing model.

developed scalar spectrum, the scalar dissipation rate, ϵ_ξ , is related to the turbulent frequency, ϵ/k, by

$$\epsilon_\xi = C_\varphi \langle \xi'^2 \rangle \frac{\epsilon}{k} \tag{21}$$

where $C_\varphi = 2$,[62] and ϵ and k are the turbulent dissipation rate and kinetic energy, respectively. The chemical source terms in eq 16 for the solute and crystals are substituted with the right-hand side of eq 12 along with the appropriate nucleation and growth kinetics that are not limited by micromixing.[94] For the case of unseeded crystallization, the micromixing terms for the crystals are zero.

Nucleation and Growth Kinetics. The solubility, c^*, of paracetamol in an acetone−water mixture at 16 °C is given by[95]

$$c^* \text{ (kg of solute/kg of solvents)} = -(5.01902 \times 10^{-12})w^6 + (1.69767 \times 10^{-9})w^5 - (2.46765 \times 10^{-7})w^4 + (2.19262 \times 10^{-5})w^3 - (1.27018 \times 10^{-3})w^2 + (3.42614 \times 10^{-2})w + 7.96086 \times 10^{-2} \tag{22}$$

or

$$c^* \text{ (kg of solute/m}^3) = -(7.56719 \times 10^{-9})w^6 + (2.52296 \times 10^{-6})w^5 - (3.32604 \times 10^{-4})w^4 + (2.33867 \times 10^{-2})w^3 - 1.01740w^2 + (2.33555 \times 10^{1})w + 6.08849 \times 10^{1} \tag{23}$$

where w is the antisolvent mass percent on a solute-free basis. The kinetic rates of primary nucleation and growth of paracetamol in an acetone−water mixture at 16 °C were approximated from the experimental data given by Granberg et al.[12] In this work, we assume that the experiments in this publication were performed under well-micromixed conditions. The primary nucleation rate, B, is expressed as

$$B \text{ (no. of nuclei/(s m}^3)) = (8.56080 \times 10^8) \times \exp\left\{ -1.22850 \times 10^{-3} \frac{\left[\ln\left(\frac{c_s \text{ (kg of solute/m}^3)}{c^* \text{ (kg of solute/m}^3)}\right)\right]^3}{\left[\ln\left(\frac{c \text{ (kg of solute/kg of solvents)}}{c^* \text{ (kg of solute/kg of solvents)}}\right)\right]^2} \right\} \tag{24}$$

where c_s is the density of the crystal and c is the supersaturated solute concentration.

For crystal growth kinetics, Karpinski[96] discussed the importance of using the two-step crystal growth model that describes the crystal growth as the diffusion of solute molecules to the crystal surface followed by the arrangement of solute molecules into the crystal lattice. It was shown that the two-step growth model has a better accuracy than the overall kinetic growth equation. The diffusion layer model proposed by Nyvlt et al.[97] described crystal growth into the following steps (see Figure 2):

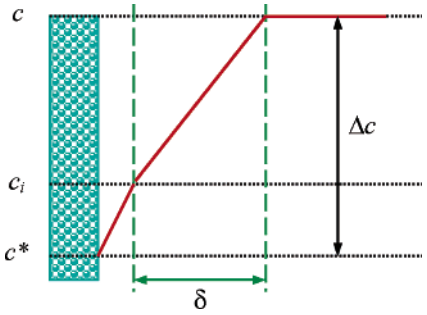

Figure 2. Diffusion layer growth model (Nyvlt, 1985).

1. Transfer of solute from the bulk solution to the diffusion layer.
2. Diffusion of the solute through the diffusion layer, whose thickness depends on the hydrodynamic conditions in the solution.
3. Incorporation of the solute molecules into the crystal lattice.

The diffusion rate across the diffusion layer can be written as

$$\frac{dm_c}{dt} = k_d A_c (c - c_i) \tag{25}$$

where dm_c/dt is the solute flux across the area A_c and k_d is the mass transfer coefficient. The concentration of species in the bulk phase of the supersaturated solution is c, and c_i is the interfacial concentration between the Volmer boundary layer and the diffusion layer. The rate of incorporation of solute into the crystal lattice can be written as

$$\frac{dm_c}{dt} = k_i A_c (c_i - c^*)^i \tag{26}$$

where k_i is the integration rate constant and i is an exponent whose value, between 1 and 2, depends on the surface integration mechanism. Equations 25 and 26 can be combined to eliminate c_i. For $i = 1$

$$\frac{dm_c}{dt} = \left(\frac{1}{k_d} + \frac{1}{k_i}\right)^{-1} A_c (\Delta c) \tag{27}$$

where $\Delta c = c - c^*$ is the supersaturation. For $i = 2$

$$\frac{dm_c}{dt} = A_c \frac{1}{2k_i/k_d^2}\left(1 + \frac{2k_i}{k_d}\Delta c - \sqrt{\frac{4k_i}{k_d}\Delta c + 1}\right) \tag{28}$$

For the case of undersaturation (negative Δc), the dissolution of crystals is a result of mass transfer:[1]

$$\frac{dm_c}{dt} = k_d A_c \Delta c \tag{29}$$

Equations 28 and 29 can be expressed as a linear growth rate G by the relation[98]

$$\frac{1}{A_c}\frac{dm_c}{dt} = 3\frac{k_v}{k_a}\rho_c \frac{dr}{dt} = 3\frac{k_v}{k_a}\rho_c G \tag{30}$$

where k_v and k_a are the volume and area shape factors,

respectively. An expression similar to eq 28 had been proposed by Mersmann et al.,[99] and it has been widely used.[32,42,100,101] Assuming that the crystal growth given by Granberg et al.[12] is measured without mass transfer limitations, the integration rate constant is

$$k_i\,(\mathrm{kg/(m^2\ s\ (kg/m^3)^2)}) = (1.95 \times 10^{-7})w - 7.35 \times 10^{-6} \qquad (31)$$
$$w \geq 30\%$$

Average values of the shape factors, $k_v = 0.605$ and $k_a = 4.63$, are assumed in the computations.

To determine the solid−liquid mass transfer coefficient, the Frossling equation can be applied for conditions of forced convection in steady flows.[1,102] For particle−liquid mass transfer in agitated systems, various authors have applied the Kolmogoroff theory of local isotropic turbulence in the mass transfer coefficient correlations.[103−107] For microparticles, whose largest size dimension is smaller than Kolmogoroff's length scale, Armenante and Kirwan[108] proposed and validated that the turbulent contribution to mass transfer is by the boundary layer development resulting from the exchange of microparticles among decaying eddies, which can be characterized by

$$Sh = 2 + 0.52Re^{0.52}Sc^{1/3} \qquad (32)$$
$$d_p \leq \lambda_k = (\nu^3/\epsilon)^{0.25}$$

where $Sh = k_d d_p/D$, $Re = \epsilon^{1/3} d_p^{4/3}/\nu$, and $Sc = \nu/D$. The particle size is d_p, ν is the kinematic viscosity, and D is the laminar diffusivity, which is approximated as 10^{-9} m/s^2.[109] For macroparticles, the correlation proposed by Levins and Glastonbury[107] can be applied. It was suggested that the mass transfer occurs predominantly by a slip velocity mechanism with some contribution from unsteady-state transfer:

$$Sh = 2 + 0.5Re^{0.62}Sc^{1/3} \qquad (33)$$
$$d_p > \lambda_k$$

Both of these correlations were developed for an agitated vessel using the overall power input per unit mass to represent ϵ. However, the localized energy dissipation rate will be used in this work.[110,111] The two-step growth rate expression is size-dependent as the mass transfer coefficient is a function of particle size.

For this crystallization system, only the kinetic parameters for primary nucleation and growth have been reported in the literature.[12] Hence, the goal of the simulations is to gain insights into how hydrodynamics affect crystal nucleation and growth. Agglomeration, breakage, and secondary nucleation for this system can be minimized by controlled seeding or by adjusting some of the operating parameters such as the agitation speed and antisolvent addition rate, as discussed by Fujiwara et al.[112] and Yu et al.[113,114] If more complex crystallization kinetic parameters were made available, then a wider range of operating conditions could be simulated.

Effective Viscosity of Suspension. It is possible to incorporate the semidiscretized PBE to compute the CSD with the multiphase Eulerian model available in CFD codes. A direct approach would be to specify the crystals in each grid cell ($r_{j-1/2}$ to $r_{j+1/2}$) as a discrete solid phase with an average size in the same range. However, the Eulerian model requires much more intensive computations, since a separate set of conservation equations has to be solved for each discrete phase. In this work, a simpler approach was used by treating the suspension as a pseudo-homogeneous phase with a spatial variation in the effective viscosity based on the localized suspension density. Numerous effective viscosity expressions for suspensions, valid for different ranges of solids concentration, can be found in the rheology literature, with most work extending from the Einstein equation, which is valid for uniform spheres at low solids concentration (<10%):[89,115,116]

$$\eta = \eta_s(1 + 2.5\phi) \qquad (34)$$

where η is the viscosity of the suspension, η_s is the viscosity of the suspending medium, and ϕ is the volume fraction of the solid phase. Many of the expressions for effective viscosity reduce to the Einstein equation in the limit of dilute suspension, which applies to organic crystals with low solubility. A significant amount of effort has also been put in to address the effects of particle size distribution and shape.[117−122] Except for rods and disks with large aspect ratios that can dramatically increase the effective viscosity even at low solids concentration, the increase in viscosity and its sensitivities to the particle shape, particle size distribution, and particle−particle interaction are insignificant at low solids concentration (≪10% volume fraction).[89] As such, the Einstein equation remains valid in this work, as the suspension is sufficiently dilute (<4%) and no needles or thin plates are formed.

Results and Discussion

Validation of High-Resolution Central Scheme. To assess the accuracy of the high-resolution central scheme in solving the PBE (written on a mass basis), it was applied to the well-mixed case of antisolvent crystallization of paracetamol in an acetone−water mixture. Equation 12, without the external coordinate terms, was solved for nucleation and size-independent growth using the ODE solver in Matlab 6.1. The nucleation rate expression was eq 24, while Granberg et al.[12] fit the growth rate expression

$$G(\mathrm{m/s}) = k_g(\Delta c\ (\mathrm{kg\ of\ solute/kg\ of\ solvents}))^g \qquad (35)$$

to experimental data, with the kinetic constants

$$k_g\,(\mathrm{m/(s\ (kg\ of\ solute/kg\ of\ solvents)^g)}) = -(1.60 \times 10^{-10})w^3 + (5.59 \times 10^{-8})w^2 - (2.10 \times 10^{-6})w + 6.14 \times 10^{-5} \qquad (36)$$

and

$$g = -(1.11 \times 10^{-4})w^2 + (1.02 \times 10^{-2})w + 1.43 \qquad (37)$$

In this well-mixed validation run, a 1 L vessel was initially half-filled with saturated solution of 65% by mass water and antisolvent added at a constant rate over 1 h to fill the vessel (i.e., direct addition). As shown in Figure 3, the zeroth through seventh order moments of the CSD computed from eq 12 for various Δr values are compared to those obtained from the method of moments. For $\Delta r = 1\ \mu$m, the moments agree well and, as Δr increases, the overestimation of the higher order moments increases due to numerical diffusion, which depends on Δr. Figure 4 shows the final CSD at the end of the batch. Small numerical diffusion is observed, with the absence of nonphysical oscillations.

Effects of Agitation Rate. This section illustrates the capability of the coupled CFD-PBE-PDF approach through the investigation of the effects of agitation rate on the CSD. Fluent

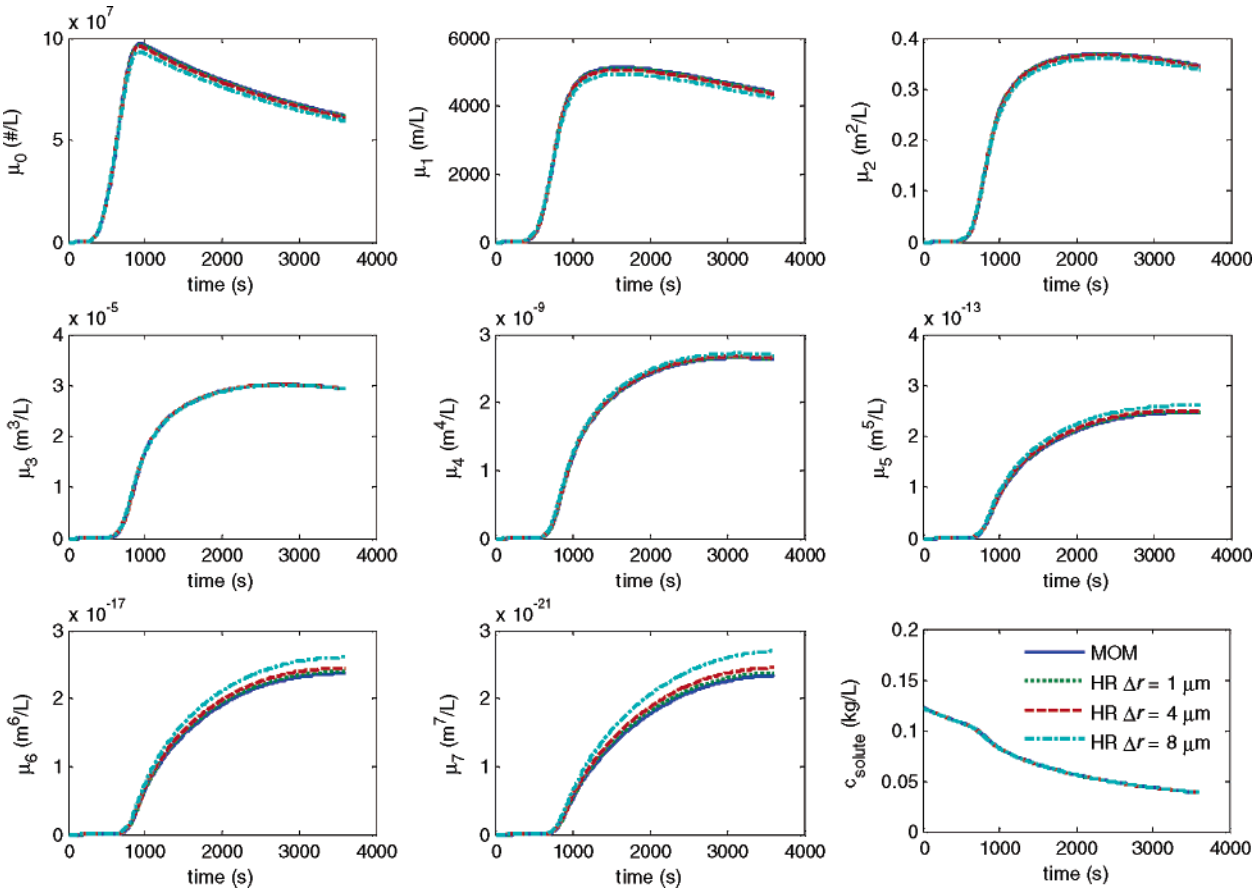

Figure 3. Zeroth through seventh order moments and solute concentration from the method of moments (MOM) and the high-resolution central scheme (HR) (eq 12) for various Δr.

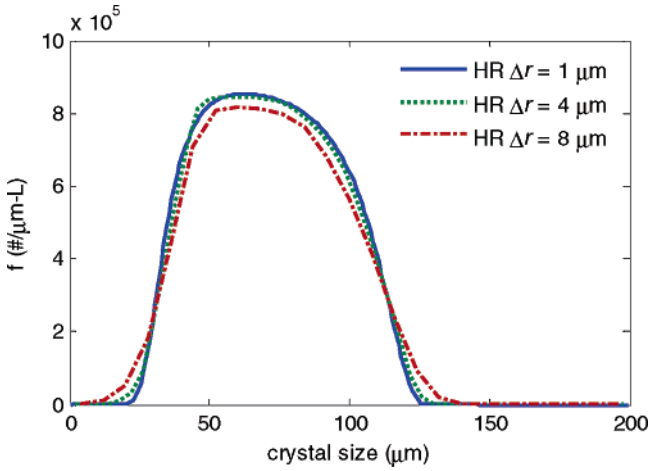

Figure 4. CSD from high-resolution central scheme (HR) (eq 12) for various Δr.

6.1.22 (Fluent Inc., Lebanon) was employed as the CFD solver, which solves the Reynolds-averaged Navier−Stokes (RANS) and conservation equations (see Appendix). The 2D axisymmetric mesh for the 1 L cylindrical vessel was generated using Gambit 2.2 (Fluent Inc., Lebanon). The turbulence in the vessel was modeled by the realizable $k-\epsilon$ model (see Appendix) with standard wall functions, while the impeller (Lightnin A200), placed a quarter of the vessel height from the bottom, was modeled by fixed velocity data[123,132] for simplicity. A steady-state flow field was first obtained for the fluid in the half-filled vessel, where $p_2 = 1$, before the introduction of the feed. The addition of the feed was modeled by a mass and p_1 source located at the feed point, corresponding to the feed flow rate, along with a momentum source to capture the downward injection. The feed rate was determined by the constant flow rate required to fill the other half of the vessel in a 1 h batch time. The rise in liquid level was modeled using a dynamic mesh by the constant height dynamic layering method,[124] in which computational cells were added adjacent to the moving boundary. The rate at which the boundary of the liquid surface moved was computed on the basis of the addition rate of the antisolvent. The additional equations described in the previous section were included into the CFD algorithm through user-defined functions, and the additional transport equations were solved as user-defined scalars.[125] All CFD simulations were carried out on a Dell PowerEdge Linux cluster with an Intel Xeon 3.2 GHz processor.[133] Here, antisolvent crystallization by the direct addition mode, similar to the system described in the well-mixed case, was modeled. The PBE was discretized into 40 grid cells with $\Delta r = 8$ μm. Each simulation, for a batch time of 1 h, took approximately 5 days to complete on a single CPU. All simulation runs for this paper can be run in parallel on a modest-sized Linux cluster (with each simulation run sent to a different processor). Further, the time for each simulation run can be reduced by a factor of ∼10 on such a cluster by using the parallelization capability in Fluent.

Figure 5 shows that the segregation of the feed and the initial solution, on the basis of the three-environment micromixing model, only occurs for a very short time (<10 s), and the reduction of segregation is faster at a higher agitation rate. The initial mixing has small regions of mixed solution (environment 3) with equal proportions of the solution and the antisolvent ($\langle\xi\rangle_3 = 0.5$), as shown in Figure 6, with localized regions of

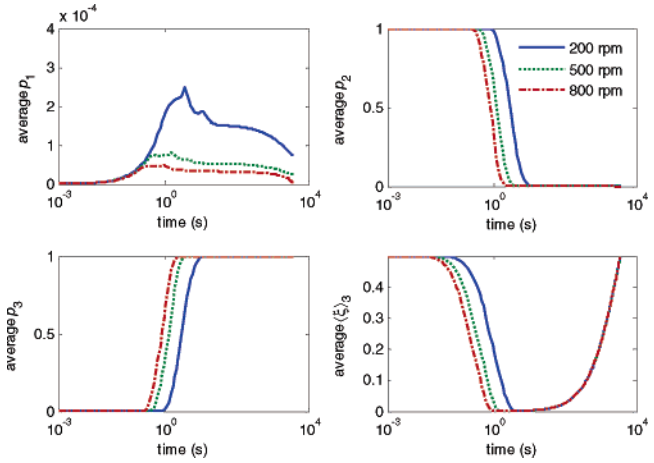

Figure 5. Volume-averaged p_1, p_2, p_3, and $\langle\xi\rangle_3$ values for various agitation rates.

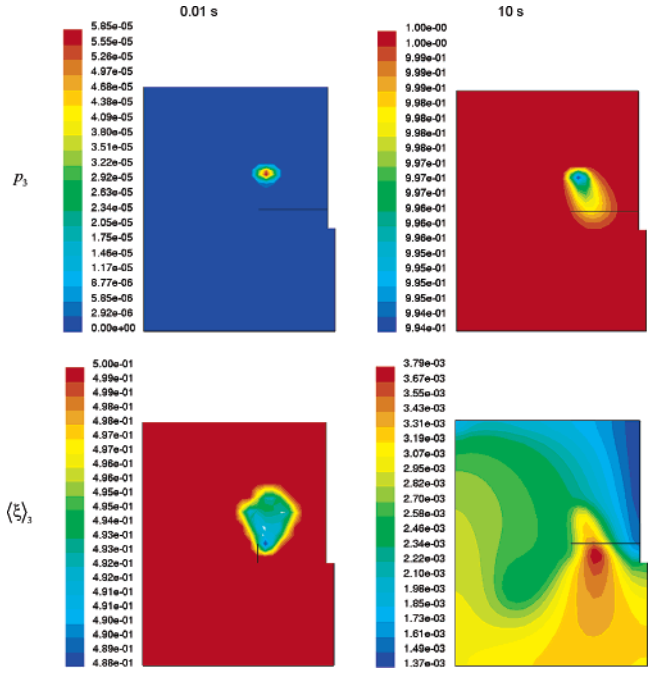

Figure 6. Spatial distributions of p_3 (mixed) and $\langle\xi\rangle_3$ at 500 rpm during initial mixing.

high supersaturation and rapid nucleation and growth rates (see Figures 8−11). Subsequently, the mixed environment extends throughout the vessel, with its major proportion being the initial solution in the vessel ($\langle\xi\rangle_3 \rightarrow 0$). The amount of antisolvent in environment 3 increases throughout the batch ($\langle\xi\rangle_3 \rightarrow 0.5$). This mixing sequence, as shown in Figure 7, results in a drop in antisolvent composition, supersaturation, and thus nucleation and growth rates, in the mixed environment, which then slowly increases with time. This is followed by the supersaturation going through a maximum (at t = 440 s for 500 rpm) and decreasing due to consumption of solute for crystal growth after a substantial amount of nuclei has formed.

Figure 12 shows the evolution of CSD during the first few minutes and throughout the entire batch at 500 rpm. Due to the initial micromixing effects, small amounts of crystals are formed, with lower agitation speeds resulting in more crystals due to slower micromixing (plot not shown). The nucleation and growth rates at the inlet drop quickly during the first few seconds (see Figures 10 and 11), after which the crystals grow with increasing growth rate (see left-hand plot in Figure 12). Such

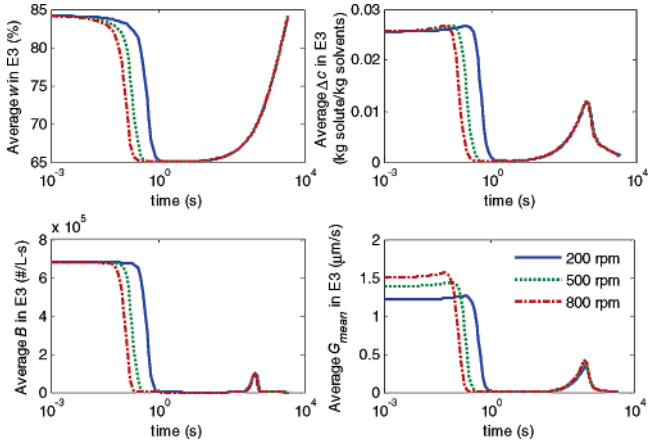

Figure 7. Volume-averaged antisolvent mass percent (w), supersaturation (Δc), nucleation rate (B), and mean growth rate of crystals of all sizes (G_{mean}) in the mixed environment 3 (E3) for various agitation rates.

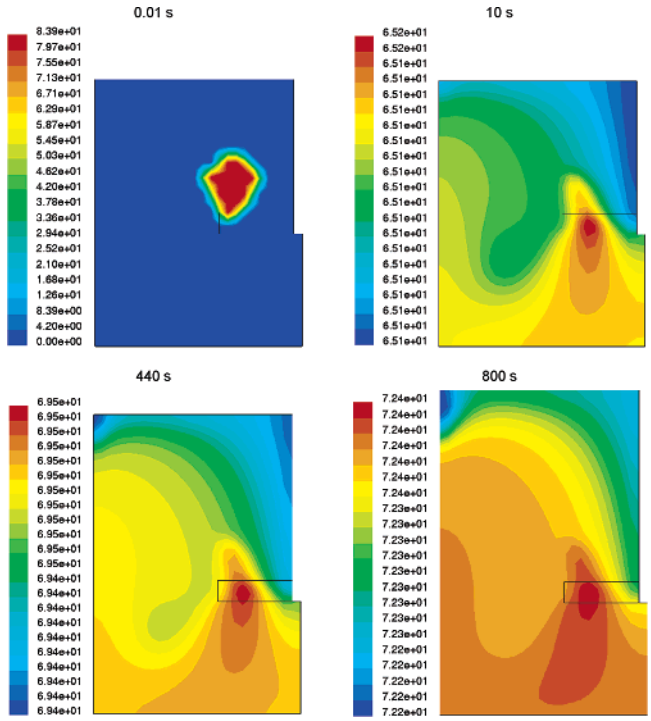

Figure 8. Spatial distribution of w (antisolvent mass percent) in environment 3 at 500 rpm for various times.

crystals formed during the initial contact of the solution and the antisolvent have been observed in some experiments[15] and do not represent the detection of a metastable limit for the overall solution. It is not surprising to observe higher growth rates at the impeller region due to higher turbulence (Figure 11). Higher growth rates are observed for higher agitation rates (see Figure 7), due to the reduction of mass transfer limitations on crystal growth. Consequently, the faster desupersaturation at higher agitation results in lower overall nucleation rates (Figure 7). This explains the final CSD (at the end of 1 h) for different agitation rates, in which fewer and slightly larger crystals are obtained with higher agitation rates (see Figure 13).

The dependence of the final CSD on agitation rate is consistent with the experimental results of Kim et al.,[126] where the crystal size of titanium(IV) oxide formed by a supercritical reaction increased with midrange stirring rate. Torbacke and Rasmuson[127] also report an increase in product mean size with

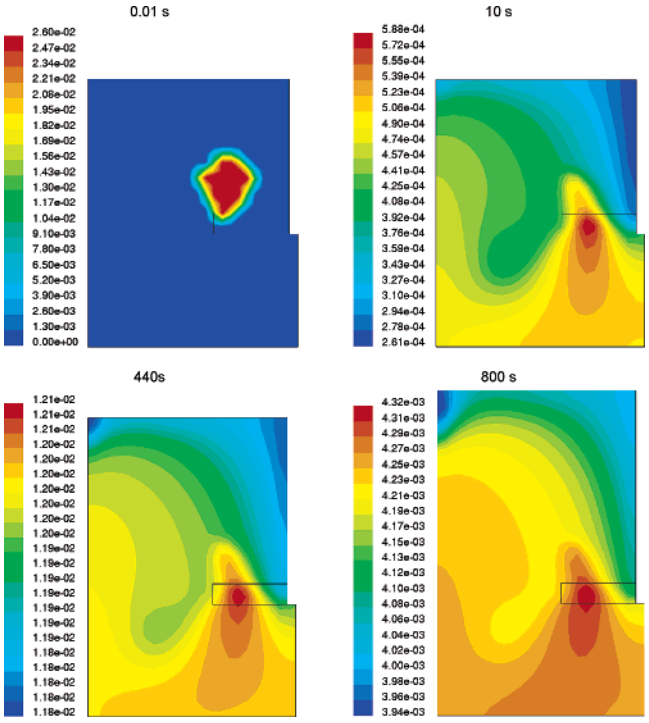

Figure 9. Spatial distributions of supersaturation Δc (kg of solute/kg of solvents) in environment 3 at 500 rpm for various times.

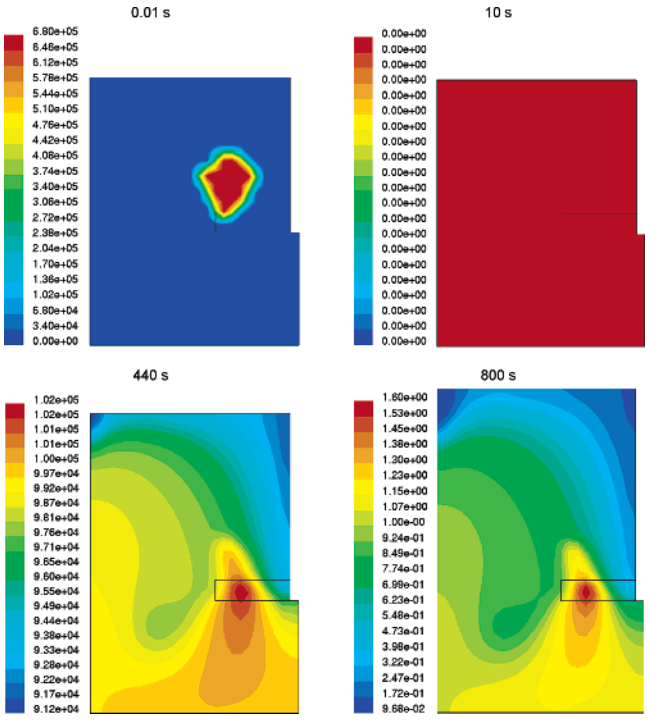

Figure 10. Spatial distributions of the nucleation rate B (no./(L s)) in environment 3 at 500 rpm for various times.

stirring rate for semibatch reaction crystallization of benzoic acid. However, no influence of stirring speed on the mean size of nanoparticles formed was observed in the experimental study of drowning out of ethylcellulose.[18] For the crystallization of griseofulvin by compressed carbon dioxide as an antisolvent,[128] and the salting out of $KAl(SO_4)_2$,[17] it was experimentally observed that the mean crystal size decreased with increasing stirring rate. Such opposing observations can be attributed to the different kinetics of each individual system. A recent

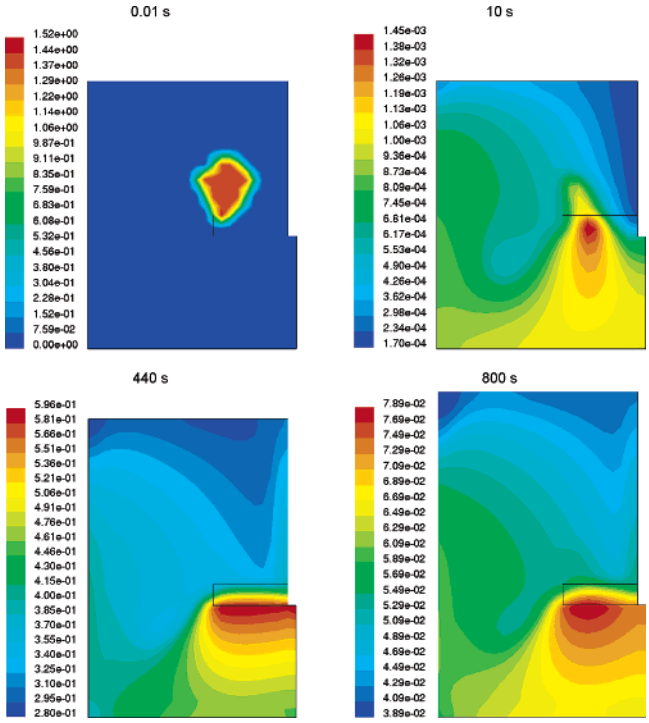

Figure 11. Spatial distributions of the mean growth rate G_{mean} (μm/s) in environment 3 at 500 rpm for various times.

publication on the paracetamol−acetone−water system by Yu et al.[113] reports that the mean particle (crystals and agglomerates) size increases and subsequently decreases with mixing speed. However, no direct comparison with the crystal size distribution can be made, due to the high degree of agglomeration at the lower mixing speeds and higher antisolvent addition rates. The authors of that paper loaned us the crystal samples from their experiments, and the larger, less agglomerated crystals were sieved out and measured under an optical microscope. It can be seen from Figure 14 that larger crystals were obtained at a higher agitation rate, consistent with the simulation results shown in Figure 13.

Effects of Addition Mode. As noted by Midler et al.,[5] reverse addition (addition of saturated solution to antisolvent) is used in the pharmaceutical industry to crystallize small particles. This addition mode was used in the crystallization studies by Kim et al.,[21] Plasari et al.,[18] and Shin and Kim.[19] To the authors' knowledge, the comparison between the effects of both addition modes has yet to be extensively studied. Here, the reverse addition mode was modeled with the same volumes of saturated solution and antisolvent as the direct addition case. This simply involved switching the concentrations in environments 1 and 2.

The time profiles of the average antisolvent composition, supersaturation, and nucleation and growth rates in environment 3 during the initial contact of the feed solution and the antisolvent are the same as the direct addition case (see Figure 15). Subsequently, during reverse addition the excessive dilution of the saturated solution by the antisolvent results in undersaturation and dissolution of the crystals formed at the initial contact (see Figure 16). For most of the crystallization the supersaturation at longer times during reverse addition is not as high as in direct addition, while the peak nucleation rate is significantly higher (see Figure 15). This is a result of the dependence of the nucleation and surface integration rates on solvent composition. In the paracetamol−acetone−water system, the nucleation and surface integration rates increase with

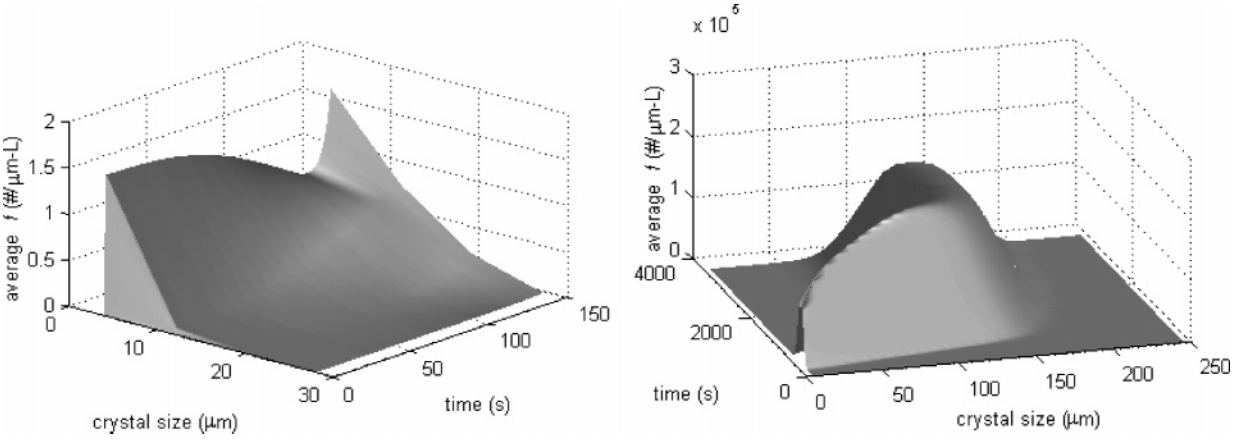

Figure 12. Evolution of the volume-averaged CSD at 500 rpm.

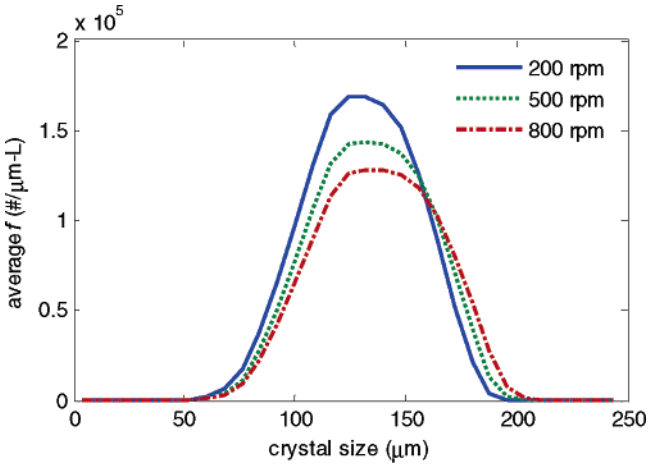

Figure 13. Final volume-averaged CSD for various agitation rates (direct addition).

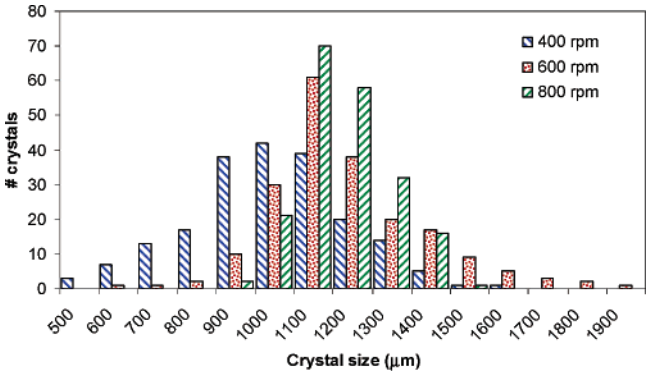

Figure 14. Crystal size distribution of paracetamol crystals obtained from Yu et al.[113] for an antisolvent addition rate of 2 g/min for various agitation rates. The larger and less agglomerated crystals were obtained by sieving (600 μm sieve), and the lengths of the longest axis of the single crystals (200 crystals total) were measured under an optical microscope (Olympus BX51).

increasing antisolvent composition. During reverse addition, a high antisolvent composition is achieved, which results in the formation of a larger number of nuclei and slower mean growth rates (see Figure 15). Consequently, the final CSD for the reverse addition mode, shown in Figure 17, has more crystals of significantly smaller size.

Effects of Scale-Up. The scale-up of crystallizers has long been a challenge for the pharmaceutical industry. The coupled algorithm enables the investigation of the effects of scale-up.

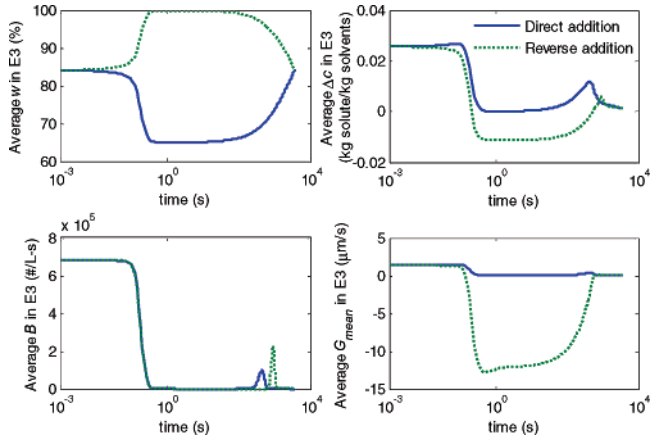

Figure 15. Volume-averaged antisolvent mass percent (w), supersaturation (Δc), nucleation rate (B). and mean growth rate (G_{mean}) in environment 3 (E3) at 500 rpm for direct and reverse addition modes.

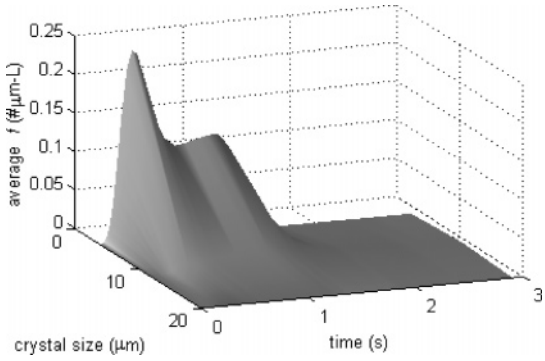

Figure 16. Evolution of volume-averaged CSD at 500 rpm for reverse addition.

Here, the 1 L vessel was scaled up to 125 L while its geometric similarity was maintained. The impeller speed, based on 500 rpm for the small scale, was scaled up according to two common scale-up rules: (i) constant tip speed (100 rpm) and (ii) constant power per unit volume (171 rpm).[27,129] The simulations for the scale-up studies for direct addition were performed for 20 min of batch time, after which the change in CSD was minimal, due to slow growth for the rest of the batch.

As shown in Figures 18 and 19, the dispersion of the feed solution is less effective on a larger scale for both scale-up criteria. By comparison of the spatial plots for the 1 L scale with both scale-up cases for the 125 L scale (not shown) at the time of highest supersaturation (t = 440 s), somewhat higher

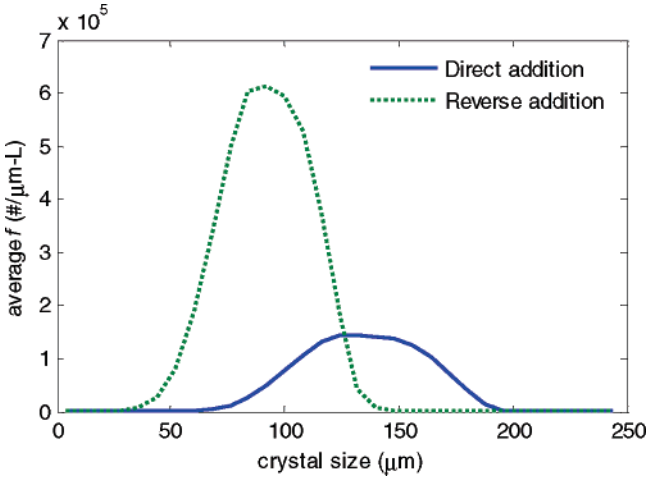

Figure 17. Final volume-averaged CSD at 500 rpm for direct and reverse addition modes.

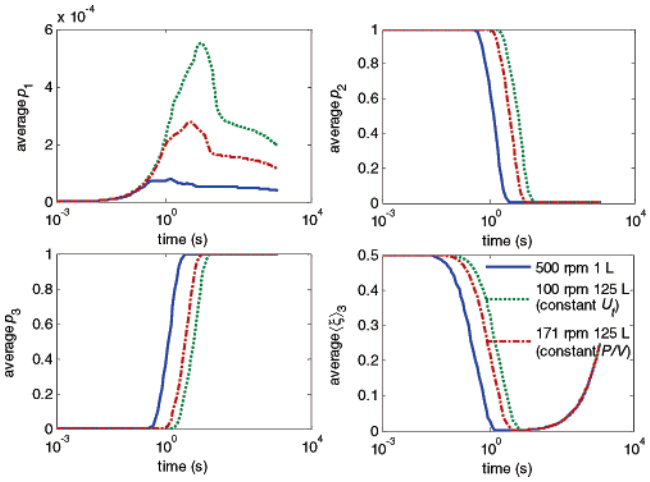

Figure 18. Volume-averaged p_1 (feed), p_2 (initial solution), p_3 (mixed), and $\langle\xi\rangle_3$ values for scale-up based on constant tip speed (U_t) and constant power per unit volume (P/V).

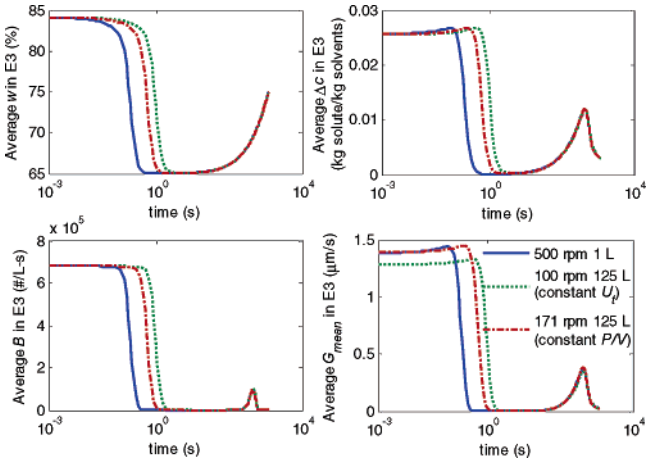

Figure 19. Volume-averaged antisolvent mass percent (w), supersaturation (Δc), nucleation rate (B), and mean growth rate (G_{mean}) in the mixed environment 3 (E3) for scale-up based on constant tip speed (U_t) and constant power per unit volume (P/V).

inhomogeneities in the antisolvent composition, the supersaturation, and the nucleation rate can be observed for the large vessel. The difference in spatial variation of the growth rate is a consequence of the spatial distribution of the turbulent energy

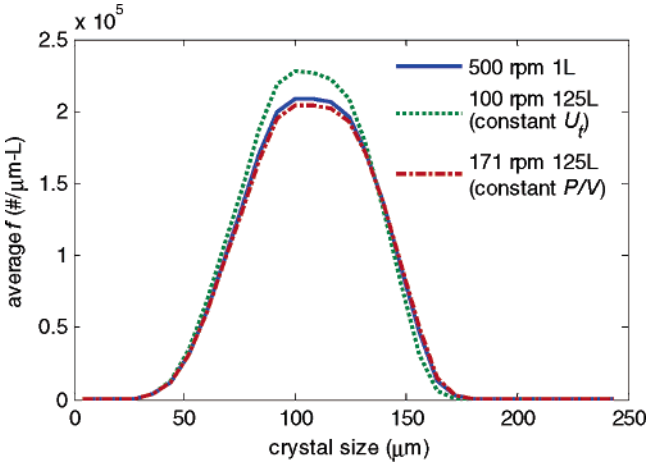

Figure 20. Volume-averaged CSD at 20 min after scale-up.

dissipation not being preserved after scale-up. The CSD obtained at the end of 20 min is shown in Figure 20, with the scale-up based on constant power per unit volume giving a better match with the CSD of the small scale. Nevertheless, no significant change in the crystal size distribution was observed on scale-up, which is consistent with the experimental findings by Torbacke and Rasmuson,[127] where the reactor size was observed to have no influence on the product mean size. More drastic differences in the CSD are expected after scale-up for crystallization systems where secondary nucleation, aggregation, and breakage are important.

Conclusion and Future Directions

The PBE, discretized along the internal coordinate using a high-resolution central scheme, and the multienvironment presumed-PDF model, which captures the micromixing effects, were integrated into a commercial CFD solver to simulate the effects of mixing on the full CSD in antisolvent crystallization. In a simulation study, larger and fewer crystals were produced when the agitation rate was increased during direct addition, and the reverse addition mode produced smaller crystals. Two rules for scaling up tip speed were compared, with constant power per unit volume resulting in a CSD closer to that of the bench-scale crystallizer.

The examples were chosen to show the effects of different operating conditions and scale on the crystal size distribution for a model system and can be extended to other systems which crystallization kinetics are known. While gaining insights into how different operating parameters can affect the crystal product quality, the design and scale-up of crystallizers to meet a desired product specification can be carried out in a more systematic way, which is a challenging problem in industrial crystallization.[130] This can reduce the number of laboratory experiments required, especially when a pharmaceutical drug is only available in small quantities in the early drug development stage, and shorten the time required to develop the manufacturing process. In this paper, we have shown how agitation rate and addition mode can be adjusted to produce a specified crystal size distribution and what scale-up rules can be used to maintain the desired crystal size distribution during scale-up.

At this point, qualitative comparisons were made with experimental data reported in the published literature, which gave some confidence that the current model can predict the trends observed in experiments qualitatively. Predicting experimental data quantitatively would require the input of accurate

parameters into the computational model. Hence, a step forward from this paper is to design experimental systems to accurately estimate the parameters in the nucleation and growth expressions and additional agglomeration, breakage, and secondary nucleation kinetics, as well as the turbulence and micromixing models.

This coupled algorithm can be further coupled with multiphase models to achieve a better accuracy for the particle flow field. This approach applies with minor modification to precipitation and cooling crystallization and, with increased computational requirements, can be extended to secondary nucleation, aggregation, and breakage processes. The additional computational time can be reduced with parallel computations and the availability of faster processors (Moore's Law). The development of this integrated model would provide a better understanding of the effects of mixing on crystallization, thus offering a more scientific basis for the design and scale-up of crystallizers. Also, it creates the opportunity to estimate crystallizer-independent crystallization kinetics, in contrast to the current literature approaches which are really estimating, whether acknowledged or not, kinetic parameters averaged over the crystallizer and, hence, are averaged over the hydrodynamics. The identification of crystallization kinetics that is independent of hydrodynamics is required for the systematic design of crystallizers of different configurations.

Acknowledgment. We acknowledge the Institute of Chemical and Engineering Sciences, Singapore, the National Center for Supercomputing Applications for the computational resources, and Mitsuko Fujiwara for input on the manuscript. The authors in Yu et al.[113] are gratefully acknowledged for providing the crystallization samples. X.Y.W. wishes to acknowledge the Singapore Agency for Science, Technology and Research for a research scholarship.

Appendix

The Reynolds-averaged Navier−Stokes (RANS) and conservation equations are briefly presented below. The reader is referred to the Fluent 6.1 User's Guide and UDF Manual for a detailed description of the parameters in the equations.[124,125]

Mass conservation (continuity) equation:

$$\frac{\partial \rho}{\partial t} + \nabla(\rho \vec{v}) = S_m \tag{38}$$

Momentum conservation equation:

$$\frac{\partial}{\partial t}(\rho \vec{v}) + \nabla\cdot(\rho \vec{v}\vec{v}) = -\nabla p + \nabla\cdot(\bar{\bar{\tau}}) + \rho \vec{g} + \vec{F} \tag{39}$$

Realizable $k-\epsilon$ turbulence model:[131]

$$\frac{\partial}{\partial t}(\rho k) + \frac{\partial}{\partial x_j}(\rho k u_j) = \frac{\partial}{\partial x_j}\left[\left(\mu + \frac{\mu_t}{\sigma_k}\right)\frac{\partial k}{\partial x_j}\right] + G_k - \rho\epsilon + S_k \tag{40}$$

$$\frac{\partial}{\partial t}(\rho \epsilon) + \frac{\partial}{\partial x_j}(\rho \epsilon u_j) = \frac{\partial}{\partial x_j}\left[\left(\mu + \frac{\mu_t}{\sigma_\epsilon}\right)\frac{\partial \epsilon}{\partial x_j}\right] + \rho C_1 S \epsilon - \rho C_2 \frac{\epsilon^2}{k + \sqrt{\nu\epsilon}} + S_\epsilon \tag{41}$$

User-defined scalar transport equation:

$$\frac{\partial}{\partial}(\rho \phi_k) + \frac{\partial}{\partial x_i}\left(\rho u_i \phi_k - \Gamma \frac{\partial \phi_k}{\partial x_i}\right) = S_{\phi k} \tag{42}$$

$$\Gamma = \left(\rho D_m + \frac{\mu_t}{\mathrm{Sc}_t}\right) \tag{43}$$

References

(1) Mullin, J. W. *Crystallization*, 4th ed.; Elsevier Butterworth-Heinemann: Oxford, U.K., 2001.
(2) Wey, J. S.; Karpinski, P. H. In *Handbook of Industrial Crystallization*, 2nd ed.; Myerson, A. S., Ed.; Butterworth-Heinemann: Boston, 2002; pp 231−248.
(3) Lindrud, M. D.; Kim, S.; Wei, C. U.S. Patent 6,302,958, 2001.
(4) Mahajan, A. J.; Kirwan, D. J. *AIChE J.* **1996**, *42*, 1801−1814.
(5) Midler, M.; Paul, E. L.; Whittington, E. F.; Futran, M.; Liu, P. D.; Hsu, J.; Pan, S.-H. U.S. Patent 5,314,506, 1994.
(6) am Ende, D. J.; Brenek, S. J. *Am. Pharm. Rev.* **2004**, *7*, 98−104.
(7) Leung, S. S.; Padden, B. E.; Munson, E. J.; Grant, D. J. W. *J. Pharm. Sci.* **1998**, *87*, 501−507.
(8) Borissova, A.; Dashova, Z.; Lai, X.; Roberts, K. J. *Cryst. Growth Des.* **2004**, *4*, 1053−1060.
(9) Budz, J.; Karpinski, P. H.; Mydlarz, J.; Nyvit, J. *Ind. Eng. Chem. Prod. Res. Dev.* **1986**, *25*, 657−664.
(10) Charmolue, H.; Rousseau, R. W. *AIChE J.* **1991**, *37*, 1121−1128.
(11) Doki, N.; Kubota, N.; Yokota, M.; Kimura, S.; Sasaki, S. *J. Chem. Eng. Jpn.* **2002**, *35*, 1099−1104.
(12) Granberg, R. A.; Bloch, D. G.; Rasmuson, A. C. *J. Cryst. Growth* **1999**, *199*, 1287−1293.
(13) Holmback, X.; Rasmuson, A. C. *J. Cryst. Growth* **1999**, *199*, 780−788.
(14) Kaneko, S.; Yamagami, Y.; Tochihara, H.; Hirasawa, I. *J. Chem. Eng. Jpn.* **2002**, *35*, 1219−1223.
(15) Mullin, J. W.; Teodossiev, N.; Sohnel, O. *Chem. Eng. Process.* **1989**, *26*, 93−99.
(16) Mydlarz, J.; Jones, A. G. *Powder Technol.* **1991**, *65*, 187−194.
(17) Nyvlt, J.; Zacek, S. *Collect. Czech. Chem. Commun.* **1986**, *51*, 1609−1617.
(18) Plasari, E.; Grisoni, P.; Villermaux, J. *Chem. Eng. Res. Des.* **1997**, *75*, 237−244.
(19) Shin, D. M.; Kim, W. S. *J. Chem. Eng. Jpn.* **2002**, *35*, 1083−1090.
(20) Takiyama, H.; Otsuhata, T.; Matsuoka, M. *Chem. Eng. Res. Des.* **1998**, *76*, 809−814.
(21) Kim, Y.; Haam, S.; Shul, Y. G.; Kim, W. S.; Jung, J. K.; Eun, H. C.; Koo, K. K. *Ind. Eng. Chem. Res.* **2003**, *42*, 883−889.
(22) Kitamura, M. *J. Cryst. Growth* **2002**, *237*, 2205−2214.
(23) Kitamura, M.; Nakamura, K. *J. Chem. Eng. Jpn.* **2002**, *35*, 1116−1122.
(24) Kitamura, M.; Sugimoto, M. *J. Cryst. Growth* **2003**, *257*, 177−184.
(25) Okamoto, M.; Hamano, M.; Ooshima, H. *J. Chem. Eng. Jpn.* **2004**, *37*, 95−101.
(26) Schroer, J. W.; Ng, K. M. *Ind. Eng. Chem. Res.* **2003**, *42*, 2230−2244.
(27) Green, D. In *Handbook of Industrial Crystallization*, 2nd ed.; Myerson, A. S., Ed.; Butterworth-Heinemann: Boston, 2002; pp 181−200.
(28) Paul, E. L.; Midler, M.; Sun, Y. In *Handbook of Industrial Mixing*; Paul, E. L., Atiemo-Obeng, V. A., Kresta, S. M., Eds.; Wiley: Hoboken, NJ, 2004; pp 1027−1070.
(29) Ma, D. L.; Tafti, D. K.; Braatz, R. D. *Comput. Chem. Eng.* **2002**, *26*, 1103−1116.
(30) Paul, E. L.; Tung, H. H.; Midler, M. *Powder Technol.* **2005**, *150*, 133−143.
(31) Fujiwara, M.; Nagy, Z. K.; Chew, J. W.; Braatz, R. D. *J. Process Control* **2005**, *15*, 493−504.
(32) Gerstlauer, A.; Motz, S.; Mitrovic, A.; Gilles, E. D. *Chem. Eng. Sci.* **2002**, *57*, 4311−4327.
(33) Gunawan, R.; Fusman, I.; Braatz, R. D. *AIChE J.* **2004**, *50*, 2738−2749.
(34) Haseltine, E. L.; Patience, D. B.; Rawlings, J. B. *Chem. Eng. Sci.* **2005**, *60*, 2627−2641.
(35) Hill, P. J.; Ng, K. M. *AIChE J.* **1997**, *43*, 715−726.
(36) Hounslow, M. J.; Ryall, R. L.; Marshall, V. R. *AIChE J.* **1988**, *34*, 1821−1832.
(37) Hounslow, M. J. *AIChE J.* **1990**, *36*, 106−116.
(38) Hu, Q.; Rohani, S.; Wang, D. X.; Jutan, A. *AIChE J.* **2004**, *50*, 1786−1794.
(39) Kumar, S.; Ramkrishna, D. *Chem. Eng. Sci.* **1997**, *52*, 4659−4679.
(40) Quintana-Hernandez, P.; Bolanos-Reynoso, E.; Miranda-Castro, B.; Salcedo-Estrada, L. *AIChE J.* **2004**, *50*, 1407−1417.
(41) Ma, D. L.; Tafti, D. K.; Braatz, R. D. *Ind. Eng. Chem. Res.* **2002**, *41*, 6217−6223.

(42) Motz, S.; Mitrovic, A.; Gilles, E. D. *Chem. Eng. Sci.* **2002**, *57*, 4329−4344.
(43) Puel, F.; Fevotte, G.; Klein, J. P. *Chem. Eng. Sci.* **2003**, *58*, 3715−3727.
(44) Puel, F.; Fevotte, G.; Klein, J. P. *Chem. Eng. Sci.* **2003**, *58*, 3729−3740.
(45) Wulkow, M.; Gerstlauer, A.; Nieken, U. *Chem. Eng. Sci.* **2001**, *56*, 2575−2588.
(46) Hulburt, H. M.; Katz, S. *Chem. Eng. Sci.* **1964**, *19*, 555.
(47) Jaworski, Z.; Nienow, A. W. *Chem. Eng. J.* **2003**, *91*, 167−174.
(48) Van Leeuwen, M. L. J.; Bruinsma, O. S. L.; Van Rosmalen, G. M. *Chem. Eng. Sci.* **1996**, *51*, 2595−2600.
(49) Wei, H.; Garside, J. *Chem. Eng. Res. Des.* **1997**, *75*, 219−227.
(50) Wei, H. Y.; Zhou, W.; Garside, J. *Ind. Eng. Chem. Res.* **2001**, *40*, 5255−5261.
(51) Choi, Y. J.; Chung, S. T.; Oh, M.; Kim, H. S. *Cryst. Growth Des.* **2005**, *5*, 959−968.
(52) Kramer, H. J. M.; Dijkstra, J. W.; Neumann, A. M.; Meadhra, R. O.; van Rosmalen, G. M. *J. Cryst. Growth* **1996**, *166*, 1084−1088.
(53) Kougoulos, E.; Jones, A. G.; Wood-Kaczmar, M. *Chem. Eng. Res. Des.* **2005**, *83*, 30−39.
(54) Baldyga, J.; Orciuch, W. *Chem. Eng. Res. Des.* **1997**, *75*, 160−170.
(55) Baldyga, J.; Orciuch, W. *Powder Technol.* **2001**, *121*, 9−19.
(56) Falk, L.; Schaer, E. *Chem. Eng. Sci.* **2001**, *56*, 2445−2457.
(57) Marchisio, D. L.; Fox, R. O.; Barresi, A. A.; Baldi, G. *Ind. Eng. Chem. Res.* **2001**, *40*, 5132−5139.
(58) Marchisio, D. L.; Fox, R. O.; Barresi, A. A.; Garbero, M.; Baldi, G. *Chem. Eng. Res. Des.* **2001**, *79*, 998−1004.
(59) Marchisio, D. L.; Barresi, A. A.; Fox, R. O. *AIChE J.* **2001**, *47*, 664−676.
(60) Piton, D.; Fox, R. O.; Marcant, B. *Can. J. Chem. Eng.* **2000**, *78*, 983−993.
(61) Wang, L. G.; Fox, R. O. *Chem. Eng. Sci.* **2003**, *58*, 4387−4401.
(62) Wang, L. G.; Fox, R. O. *AIChE J.* **2004**, *50*, 2217−2232.
(63) Pope, S. B. *Prog. Energ. Combust.* **1985**, *11*, 119−192.
(64) Pope, S. B. *Turbulent Flows*; Cambridge University Press: Cambridge, U.K., 2000.
(65) Henczka, M.; Baldyga, J.; Shekunov, B. Y. *Chem. Eng. Sci.* **2005**, *60*, 2193−2201.
(66) Baldyga, J.; Bourne, J. R. *Turbulent Mixing and Chemical Reactions*; Wiley: Chichester, U.K., 1999.
(67) Phillips, R.; Rohani, S.; Baldyga, J. *AIChE J.* **1999**, *45*, 82−92.
(68) Baldyga, J.; Podgorska, W.; Pohorecki, R. *Chem. Eng. Sci.* **1995**, *50*, 1281−1300.
(69) Schwarzer, H. C.; Peukert, W. *AIChE J.* **2004**, *50*, 3234−3247.
(70) Zauner, R.; Jones, A. G. *Chem. Eng. Res. Des.* **2000**, *78*, 894−902.
(71) Zauner, R.; Jones, A. G. *Ind. Eng. Chem. Res.* **2000**, *39*, 2392−2403.
(72) Zauner, R.; Jones, A. G. *Chem. Eng. Sci.* **2002**, *57*, 821−831.
(73) Kresta, S.; Anthieren, G.; Parsiegla, K. *Chem. Eng. Sci.* **2005**, *60*, 2135−2153.
(74) Alexopoulos, A. H.; Maggioris, D.; Kiparissides, C. *Chem. Eng. Sci.* **2002**, *57*, 1735−1752.
(75) Ma, D. L.; Braatz, R. D.; Tafti, D. K. *Int. J. Mod. Phys. B* **2002**, *16*, 383−390.
(76) Sha, Z. L.; Palosaari, S. *J. Chem. Eng. Jpn.* **2002**, *35*, 1188−1195.
(77) Dhanasekharan, K. M.; Sanyal, J.; Jain, A.; Haidari, A. *Chem. Eng. Sci.* **2005**, *60*, 213−218.
(78) Venneker, B. C. H.; Derksen, J. J.; Van den Akker, H. E. A. *AIChE J.* **2002**, *48*, 673−685.
(79) Braatz, R. D.; Fujiwara, M.; Ma, D. L.; Togkalidou, T.; Tafti, D. K. *Int. J. Mod. Phys. B* **2002**, *16*, 346−353.
(80) Bachalo, W. D. *Int. J. Multiphase Flow* **1994**, *20*, 261−295.
(81) Bardow, A.; Marquardt, W.; Goke, V.; Koss, H. J.; Lucas, K. *AIChE J.* **2003**, *49*, 323−334.
(82) Gladden, L. F. *Top. Catal.* **2003**, *24*, 19−28.
(83) Stanley, S. J.; Mann, R.; Primrose, K. *AIChE J.* **2005**, *51*, 607−614.
(84) Fox, R. O. *Computational Models for Turbulent Reacting Flows*; Cambridge University Press: Cambridge, U.K., 2003.
(85) Moody, E. G.; Collins, L. R. *Aerosol Sci. Technol.* **2003**, *37*, 403−424.
(86) Kurganov, A.; Tadmor, E. *J. Comput. Phys.* **2000**, *160*, 241−282.
(87) Duvigneau, R.; Visonneau, M. *Struct. Multidiscip. O.* **2004**, *28*, 195−205.
(88) Gao, X. W.; Chen, P. C.; Tang, L. *AIAA J.* **2002**, *40*, 1512−1517.
(89) Barnes, H. A.; Hutton, J. F.; Walters, K. In *An Introduction to Rheology*, Elsevier Science: Amsterdam, 1989; pp 115−139.
(90) Leveque, R. J. *Finite Volume Methods for Hyperbolic Problems*; Cambridge University Press: Cambridge, U.K., 2002.
(91) Nessyahu, H.; Tadmor, E. *J. Comput. Phys.* **1990**, *87*, 408−463.
(92) Kurganov, A.; Noelle, S.; Petrova, G. *SIAM J. Sci. Comput.* **2001**, *23*, 707−740.
(93) Randolph, A. D.; Larson, M. A. *Theory of Particulate Processes*; Academic Press: San Diego, CA, 1988.
(94) Mahajan, A. J.; Kirwan, D. J. *J. Cryst. Growth* **1994**, *144*, 281−290.
(95) Granberg, R. A.; Rasmuson, A. C. *J. Chem. Eng. Data* **2000**, *45*, 478−483.
(96) Karpinski, P. H. *Chem. Eng. Sci.* **1985**, *40*, 641−646.
(97) Nyvlt, J.; Sohnel, O.; Matuchova, M.; Broul, M. *The Kinetics of Industrial Crystallization*; Elsevier: New York, 1985.
(98) Myerson, A. S.; Ginde, R. In *Handbook of Industrial Crystallization*, 2nd ed.; Myerson, A. S., Ed.; Butterworth-Heinemann: Boston, 2002; pp 33−66.
(99) Mersmann, A.; Angerhofer, M.; Gutwald, T.; Sangl, R.; Wang, S. *Sep. Technol.* **1992**, *2*, 85−97.
(100) Gahn, C.; Mersmann, A. *Chem. Eng. Sci.* **1999**, *54*, 1283−1292.
(101) Westhoff, G. M.; Butler, B. K.; Kramer, H. J. M.; Jansens, P. J. *J. Cryst. Growth* **2002**, *237*, 2136−2141.
(102) Ohara, M.; Reid, R. C. *Modeling Crystal Growth Rates from Solution*; Prentice-Hall: Englewood Cliffs, NJ, 1973.
(103) Calderbank, P. H.; Moo-Young, M. B. *Chem. Eng. Sci.* **1961**, *16*, 39.
(104) Levich, V. G. *Physiochemical Hydrodynamics*; Prentice-Hall: Englewood Cliffs, NJ, 1962.
(105) Middleman, S. *AIChE J.* **1965**, *11*, 750−752, 760−761.
(106) Hughmark, G. A. *Chem. Eng. Sci.* **1969**, *24*, 291−297.
(107) Levins, D. M.; Glastonbury, J. R. *Trans. Inst. Chem. Eng.* **1972**, *50*, 132−146.
(108) Armenante, P. M.; Kirwan, D. J. *Chem. Eng. Sci.* **1989**, *44*, 2781−2796.
(109) Deen, W. M. *Analysis of Transport Phenomena*; Oxford University Press: New York, 1998.
(110) Levins, D. M.; Glastonbury, J. R. *Chem. Eng. Sci.* **1972**, *27*, 537−543.
(111) Mori, Y.; Sha, Z. L.; Louhi-Kultanen, M.; Kallas, J. *J. Chem. Eng. Jpn.* **2002**, *35*, 1178−1187.
(112) Fujiwara, M.; Chow, P. S.; Ma, D. L.; Braatz, R. D. *Cryst. Growth Des.* **2002**, *2*, 363−370.
(113) Yu, Z. Q.; Tan, R. B. H.; Chow, P. S. *J. Cryst. Growth* **2005**, *279*, 477−488.
(114) Yu, Z. Q.; Chow, P. S.; Tan, R. B. H. *Ind. Eng. Chem. Res.* **2006**, *45*, 438−444.
(115) Einstein, A. *Ann. Phys.* **1906**, *19*, 289−306.
(116) Einstein, A. *Ann. Phys.* **1911**, *34*, 591−592.
(117) Chang, C. Y.; Powell, R. L. *AIChE J.* **2002**, *48*, 2475−2480.
(118) Farris, R. J. *J. Rheol.* **1968**, *12*, 281−301.
(119) Mooney, M. *J. Colloid Sci.* **1951**, *6*, 162−170.
(120) Parkinson, C.; Matsumoto, S.; Sherman, P. *J. Colloid Interface Sci.* **1970**, *33*, 150−160.
(121) Phan-Thien, N.; Pham, D. C. *Int. J. Eng. Sci.* **2000**, *38*, 73−88.
(122) Sudduth, R. D. *J. Appl. Polym. Sci.* **1993**, *50*, 123−147.
(123) Marshall, E. M.; Bakker, A. In *Handbook of Industrial Mixing*; Paul, E. L., Atiemo-Obeng, V. A., Kresta, S. M., Eds.; Wiley: Hoboken, NJ, 2004; pp 257−344.
(124) *Fluent 6.1 User's Guide*; Fluent Inc.: Lebanon, NH, 2003.
(125) *Fluent 6.1 UDF Manual*; Fluent Inc.: Lebanon, NH, 2003.
(126) Kim, T. H.; Lim, D. Y.; Yu, B. S.; Lee, J. H.; Goto, M. *Ind. Eng. Chem. Res.* **2000**, *39*, 4702−4706.
(127) Torbacke, M.; Rasmuson, A. C. *AIChE J.* **2004**, *50*, 3107−3119.
(128) De Gioannis, B.; Jestin, P.; Subra, P. *J. Cryst. Growth* **2004**, *262*, 519−526.
(129) Kresta, S. M.; Brodkey, R. S. In *Handbook of Industrial Mixing*; Paul, E. L., Atiemo-Obeng, V. A., Kresta, S. M., Eds.; Wiley: Hoboken, NJ, 2004; pp 19−88.
(130) Braun, B.; Groen, H.; Tschernjaew, J. *Cryst. Growth Des.* **2004**, *4*, 915−920.
(131) Shih, T. H.; Zhu, J.; Lumley, J. L. *Comput. Methodol. Appl. M.* **1995**, *125*, 287−302.
(132) Fixed velocity data were obtained from http://www.fluentusers.com/mixsim/faq/faq5.htm and were applied as momentum and turbulence sources in the row of cells below the impeller region.
(133) http://www.ncsa.uiuc.edu/UserInfo/Resources/Hardware/XeonCluster/.

CG0503090